ORIGINAL ARTICLE

Multi-sectional SVD-based machine learning for imagery signal processing and tool wear prediction during CNC milling of Inconel 718

Tiyamike Banda[1,2] · Veronica Lestari Jauw[1] · Chuan Li[3] · Ali Akhavan Farid[1] · Chin Seong Lim[1]

Abstract

Inconel 718 possesses exceptional properties that negatively affect tool life and other key indicators of the cutting mechanism. Owing to the unprecedented failure states of carbide inserts under the synergistic impact of processing conditions and the complex superalloy's metallurgical properties, the imagery signals contain smeared noise, which affects the predictive efficiency of data analytics during tool condition monitoring (TCM). Previous studies applied image processing techniques, such as edge segmentation, detection, auto-encoders, textural, fractal, Fourier, and wavelet analysis, to extract features from tool wear signals despite being inefficient under complex wear morphology. Therefore, this study applies a more efficient data-mining analytic called the multi-sectional singular value decomposition (multi-sectional SVD) for dimensionality reduction and extraction of features from the complex imagery signals, enhancing the predictive efficiency of machine learning (ML) during TCM. To achieve this, an interrupted climb-milling of Inconel 718 was conducted at various speeds, feeds, and axial depth of cut to generate the dataset through the in-process acquisition of tool wear images, as well as measurement of the progressive VB for the PVD-TiAlN/NbN-coated carbide inserts. Then, the multi-sectional SVD-based ML was employed to process the imagery signals and extract latent features that combined with process parameters to predict VB. After validating the predicted against the actual VB values, the model yielded a mean average percentage error (MAPE) of 2.36%, indicating its effectiveness in predicting VB profile under complex flank wear morphology. Furthermore, the system was utilized to design an effective cutting condition, where the multi-stage adjustment of speed and feed was employed to reduce the VB rate in the early cutting stage.

Keywords Tool condition monitoring · Machine vision · Multi-sectional SVD · Machine learning · Signal processing

1 Introduction

Nickel-based superalloys, such as Inconel 718, are renowned for their remarkable chemical, thermal, and mechanical properties, which enable them to retain their strength through precipitation hardening of their γ' and γ'' phases at high cutting temperatures [1]. Unfortunately, such metallurgical properties also attribute to the synergistic wear mechanisms and unprecedented failure of the carbide tools, leading to fatigue crack initiation, high scrap rate, out-of-tolerance dimension, poor surface finish, and undesirable performance of the aircraft engine's structural components [2]. With tool condition monitoring (TCM) being analogous to smart machining according to industry 4.0 [3], flank wear depth (VB) is predicted online to determine the failure criteria through the utilization of optical metrology and data analytics [4]. This provides a live update of the wear states and prevents the unprecedented failure of the carbide inserts, thus minimizing machining errors to satisfy the industrial precision standards of the aerospace components during CNC milling operation [5]. Previous research applied the Gaussian kernel ridge regression (GKRR) ML model using features of the cutting speed, feed rate, depth of cut, and cutting length to optimize the rate of VB for PVD-TiAlN/NbN-coated carbide inserts during CNC milling

✉ Chin Seong Lim
ChinSeong.Lim@nottingham.edu.my

[1] Department of Mechanical, Materials and Manufacturing Engineering, University of Nottingham Malaysia, Semenyih, Malaysia

[2] Department of Mechanical Engineering, Malawi University of Business and Applied Sciences, Blantyre, Malawi

[3] School of Mechanical Engineering, Dongguan University of Technology, Dongguan 523808, China

of Inconel 718 [6]. Although this enhanced the quantitative understanding of tool wear evolution, features of the process parameters are inefficient to extrapolate real-time VB profile, especially by considering that most industries apply fixed parameters during CNC machining. Hence, researchers have been working on enhancing signal processing techniques to extract features from time-series tool wear data as direct indicators of VB evolution during machining. In the meantime, these features are not easily defined due to unprecedented failure states of most carbide inserts when milling Inconel 718, which induces the heterogeneous pixel distribution and unstructured energy layers on the tool's cutting edge, resulting in smeared noise of the imagery signals during TCM [7]. As a result, tool wear data acquired under such conditions are subjected to pre-processing for denoising, dimensionality reduction, and extraction of a feature vector, as an abstract representation of complex wear morphology during machining. Therefore, feature engineering is introduced in Machine Vision-based TCM (MV-TCM) for processing and extracting features from time-series signals to predict VB and RUL online [8–10].

Previous research has shown that classical image processing techniques, such as segmentation and edge detection, can be used to extract more detailed geometric features, such as the area, perimeter, and average width of the flank wear region, which can be used to predict VB progression during machining [11, 12]. A more related study employed auto-segmentation and edge detection to extract the average width of the wear region and predict the VB rate using a Sobel operator through the automatic wear value detection of the PVD- and CVD-coated carbide inserts during climb-milling of Inconel 718 [13]. The system achieved a mean average percentage error (MAPE) of 4.76%, with a high average precision of 96%. Owing to the complex wear geometry when machining Inconel 718, it was believed that the auto-detection and segmentation could still be improved by enhancing it with contrast limited adaptive histogram equalization and fractal analysis to enhance the extraction of area, perimeter, and fractal dimension as predominant features that can predict VB progression during machining [14]. In this way, the artificial neural network (ANN) was able to achieve a higher performance, with an accuracy and MAPE of 95.5% and 1.099%, respectively. However, the performance was also improved due to the features extracted from the side cutting edge—a complex process that works for specific types of insert geometry. In addition, the edge or contour segmentation and detection rely on the bi-modal nature of wear images, which becomes unstable for wear regions with inconsistent signal-to-noise ratio under complex wear morphology [15]. This causes under- or over-detection or segmentation of the wear region to the extent that features

extracted under such complex geometry are not reliable to extrapolate VB progression online.

To overcome this shortcoming, textural analysis is used to capture the spatial variation of pixel distribution regardless of the multi-modal nature of tool wear images during machining. For example, the gray-level co-occurrence matrix (GLCM) technique was used to extract contrast, energy, correlation, and homogeneity of the flank wear region, despite the features being undefined under different wear resolutions [16]. To improve the extraction of the multi-scale textural features on imagery signals with different resolutions, the GLCM can be enhanced with watershed, wavelet transform, and Markov random field segmentation. However, such techniques are not easily optimized, thus, techniques like marker-controlled watershed or region merging can help to reduce over-detection or segmentation of the wear region, even though they can also be affected by the wear depth during machining [17]. In this case, methods like interpolation and search techniques can help to extract reliable textural features at varying wear depths during MV-TCM [18]. Again, these methods are plagued with high computational complexity, resulting in unnecessary delays during online signal processing.

Therefore, this research proposes advanced data-mining analytics, such as principal component analysis (PCA), singular value decomposition (SVD), tensor decomposition, and deep learning, as leading-edge technology for dimensionality reduction and extraction of image features at low computational complexity [19]. However, when dealing with full-rank approximation and unique matrix decomposition under limited data, SVD is efficient in factorizing time-series tool wear images into three parts: an orthogonal matrix (U), a diagonal matrix (S), and a transposed orthogonal matrix (V), based on the hypothesis of linear algebra that a grayscale tool wear image is a 2-D matrix with pixel distribution representing rows and columns [20, 21]. Figure 1 illustrates the process of factorizing a tool wear image into three subspace learning factors: U_{AB}, S_{AB}, and V_{AB}, derived from an image matrix AB, where U_{AB} captures the basis vectors for the spatial image structure, such as edges, textures, and shapes; S_{AB} contains singular values, representing the magnitude or significance of each basis vector in U_{AB}; and V_{AB} represents the linear transformation of the original tool wear image AB onto the basis vectors of U_{AB}, along with the corresponding singular values in S_{AB}.

Furthermore, it was reported that SVD shares a fundamental similarity with Fourier analysis, in that both processes entail unitary transform or a change in basis vectors and have the capacity to approximate reduced-rank images [17]. However, SVD outperforms the standard Fourier transform in capturing the basis vectors of imagery data, as reported in [20, 21], making it a valuable tool to capture intrinsic feature patterns of the time-series tool wear
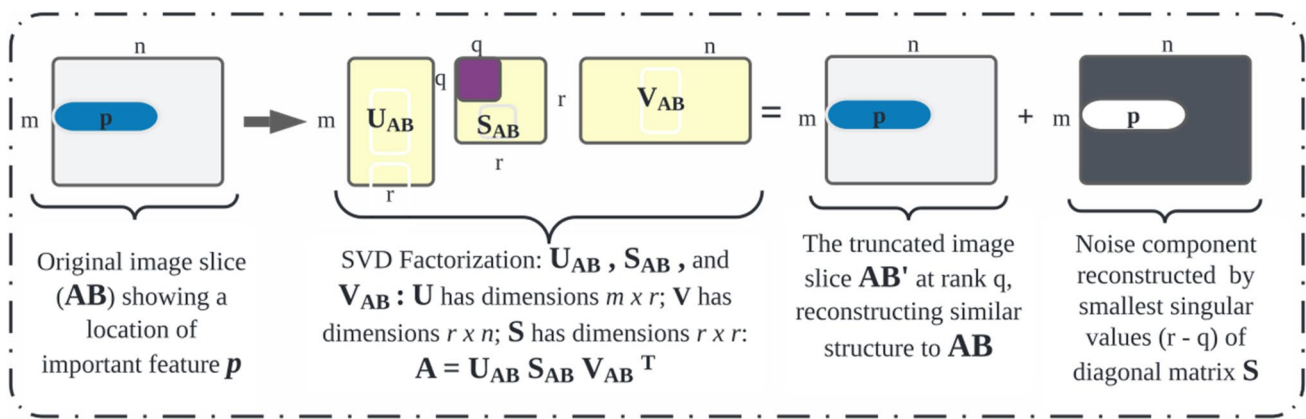
Fig. 1 Factorizing tool wear image into 3 sub-space learning factors (U_{AB}, S_{AB}, and V_{AB}) of an image matrix AB

signals during MV-TCM. It utilizes the strength of singular values (SVs) to restore energy layers of the wear region by recognizing the patterns of dominant features truncated by the largest SVs while removing the noise truncated by the smallest SVs [21]–[22]. Such a characteristic localizes the noise component orthogonal to the data signal sub-space [23], controlling two properties of imagery data: smeared noise and prevalent features. It is also worth noting that SVD does not rely on covariance matrix; thus, it provides a unique decomposition for any given image matrix and ensures no loss of information during full-rank truncation as compared to PCA, which considers an image as a single object and relies on a selected set of principle components to reconstruct the reduced-rank approximation of the original image [24]. In addition, SVD is more efficient for matrix factorization, scales well with large datasets, and yields unique solutions with a simpler abstract representation of features in the dataset as compared to tensor decomposition, which has intricate mathematical formulations and computational complexity [25]. In general, SVD has the following characteristics, which qualifies it for signal processing during MV-TCM:

Denoising: By utilizing the largest singular values to reconstruct tool wear images, SVD can separate the intrinsic features from the smeared noise while preserving the similarity structural index and failure patterns of the original wear region.
Dimensionality reduction: It effectively reduces the large dimensions of tool wear images by capturing the significant pixel information, while removing the noise component orthogonal to the data signal sub-space. This can reduce the data storage and computational complexity of ML models during MV-TCM application.
Image compression: The singular values, acquired in a new sub-space, represent the significant energy layers of each singular vector of the wear region before decom-

position. The significant feature embeddings and energy layers are localized in the first few largest singular values; thus, focusing on these values can compress an image while retaining its important structural similarity index.
Features extraction: SVD identifies the intrinsic features of the wear region by representing the distinctive geometry in U_{AB} and V_{AB} singular matrices of the truncated wear images. These functions can be considered as state-space matrices that represent the significant features for image recognition, classification, and clustering.
Computational efficiency: It factorizes the image matrix into factors in a new sub-space learning. These factors are truncated by the largest singular values to reconstruct a reduced-rank approximation without loss of significant information in the original tool wear image. The compressed image data require lower computational power to extract features for VB prediction. Hence, SVD scales well with large dataset without loss of information, substantial computational complexity, or system crushes.

Therefore, this research's significance is based on the enhancement of the powerful SVD data-mining analytic with a multi-sectioning algorithm to extract features from time-series tool wear signals as key descriptor variables of VB and RUL prediction during face milling of Inconel 718. To achieve this, small sections or sub-regions (ROIs) were generated on the flank wear region, and through the factorization by SVD, the ROIs that exhibited the highest magnitudes of the energy layers along the cutting edge were selected. The synergy of these retained ROIs resulted in a thin and tall column matrix that represented the magnitude of the highest energy layer (F_i), in the direction of the flank wear depth (VB). Furthermore, the significance of the F_i feature was substantiated by combining it with the process parameters to train an ANN for VB prediction, as well as estimation of the tools' RUL before failure. Unlike the previous systems, the multi-sectional SVD-based MV-TCM system in this

Table 1 Physical and mechanical properties of Inconel 718

Specific density	Thermal conductivity	Hardness	σ_y	σ_{UTS}	% Elongation
8.22	6.5 w/m. K	36 HRC	725 MPa	1035 MPa	30 min

Table 4 Factors and their respective levels

Level	Speed (V_c m/min)	Feed (f_t mm/tooth)	Axial depth of cut (a_p mm)
0	40	0.07	0.5
1	60	0.1	0.75
2	80	0.13	1

research was further utilized to design the promising cutting condition that minimized the rate of F_i evolution, thus, improving the performance of the carbide inserts during face milling of Inconel 718. Therefore, this study demonstrates the potential of a multi-sectional SVD for dimensionality reduction, feature extraction, and design of optimal processing conditions, which is a significant contribution to online signal processing and intelligent machining of superalloys according to Industry 4.0. As such, this research contributes significantly to the academic and scientific community by streamlining dimensionality reduction and feature selection for high-dimensional imagery signals during MV-TCM. This ensures that the most informative features are retained for predictive modeling, thereby improving interpretability by focusing on the most relevant aspects of tool wear evolution. Consequently, this approach empowers the development of more effective and interpretable predictive models capable of addressing the complexities of tool wear monitoring in challenging CNC machining domains.

2 Methodology

2.1 Materials and experiment

The goal of the experiment was to gather time-series tool wear data for training a multi-sectional SVD for features extraction and ANN for VB and RUL prediction. A DMC 835 V-DECKEL MAHO CNC milling machine was utilized to cut an Inconel 718 block ($100 \times 25 \times 50$ mm) using the multi-layer PVD-TiAlN/NbN-coated carbide inserts (made by SECO tools, Sweden) with the help of mineral oil-based cutting fluid to reduce friction and heat during machining. The cutting insert had an approach angle (k) of 45°, a rake angle (γ) of 18°, a radial angle (α) of 8°, and a radial depth

of cut (a_e) of 12.5 mm during the down milling operation. A 32-mm diameter cutter (R220.53–0032-09-4A, arbor mounting) with 4 slots for 4 wear inserts was used during the experiment. The physical, chemical, and mechanical properties of Inconel 718 used in this research are shown in Tables 1 and 2. In addition, Table 3 shows the micro-mechanical properties of multi-layer PVD-TiAlN-NbN-coated inserts applied in this research. The experiment used a full factorial design based on the levels of process parameters listed in Table 4.

Figure 2 illustrates the methodology of developing an ML-based MV-TCM system, outlining a systematic approach to enhance feature extraction and tool wear prediction during TCM. It involves data collection from the CNC machining process of Inconel 718, data pre-processing, followed by feature extraction and dimensionality reduction to capture relevant information and reduce computational complexity. Additionally, it involves ML model development, training/validation, and integration into the in-process MV-TCM system. During the experiment, the CNC machine was stopped at an incremental cutting length of 400 mm (for the lowest and medium speed) and 200 mm (for the highest speed). The inserts were removed from the cutter, placed on a fixture, and then examined under an Olympus optical microscope (Olympus U-MSSP4, BX53M, 1000× magnification, Tokyo, Japan) to measure the actual VB using a magnification scale of 50×. The experiment used failure criteria based on the ISO 8688 standard, with a maximum VB threshold of 500 μm [26]. It is also worth noting that this largest VB criterion was selected to ensure the multi-sectional SVD-based ML model was robust enough to extrapolate the VB progression outside the average critical threshold of 300 μm. To further substantiate the research findings,
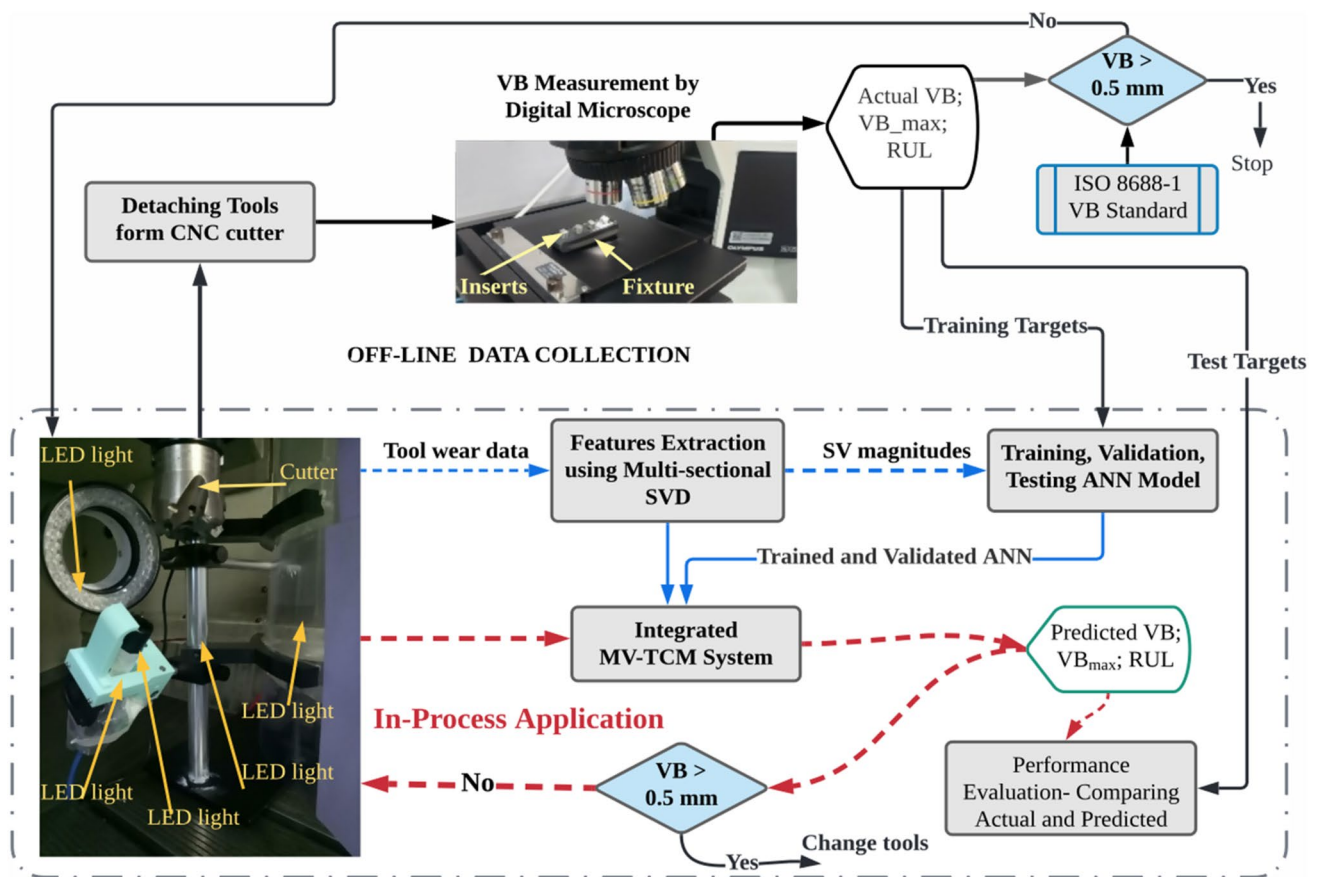
Table 2 Chemical composition of Inconel 718

Chemical	C	Cr	Mo	Ti	Ni	Nb	Al	Cu	Si	Fe
Weight (%)	0.08	21	3.3	1.15	55	5.5	0.8	0.3	0.1	12.8

Table 3 Micro-mechanical properties and composition of PVD-TiAlN-NbN-coated inserts

Hardness	T_{OXD}	μ_f	Thickness	Ra	EDX composition
2800	800 °C	70	2–4 μm	2.105 μm	N (69.6%), Nb (28%), Ti (1.5%), Al (0.82%)

Fig. 2 The methodology of developing an ML-based MV-TCM system

the actual RUL was computed by subtracting the incremental cutting time (*t, equivalent to L = 200 or 400 mm*) from the maximum time (*T*) of each experimental condition (*RUL = T- t*) as an empirical indicator of tool life during machining. The actual VB and RUL had the measurement error of *34* μm and *23* μm during experiment. Out of 27 experiments (506 flank wear images), 24 experiments (405 images) were used to train the multi-sectional SVD-based ANN model for VB and RUL prediction. The remaining 3 experiments (101 images), selected from a condition of $V_c = 40$ *m/min*, $f_t = 0.13$ *mm/tooth*, and $a_p = 1$ *mm*, were used to validate the model.

Furthermore, the trained multi-sectional SVD-based ML model was applied during MV-TCM for in-process prediction of VB progression at an optimal processing condition ($V_c = 40$ *m/min*, $f_t = 0.08$ *mm/tooth*, and $a_p = 0.9$ *mm*), designed by a GKRR model using similar data in [6]. At this condition, the F_i magnitude was correlated with process parameters to establish the limiting threshold values at different VB levels (early, uniform, critical, and failure regions), which were then utilized to determine the MV-TCM stopping criteria during

in-process utilization. During this experiment, the flank wear images were captured online using an industrial camera (Baumer, VCXU-65 M.R, 1/1.8″ CMOS sensor, 3072 × 2048 resolution, 47 fps, Vitals Vision Technology, Singapore) and a telecentric lens (APT08-65, 0.8 × magnification, 1/1.8″ sensor, Vitals Vision Technology, Singapore), which were oriented at a 45° angle relative to the CNC spindle axis. The camera and lens were set at a working distance of 65 mm, which was also a focal coordinate of a CNC G-code for optimal image capturing. Owing to the poor resolution of wear images captured by the MV-TCM system, data was then transferred to the multi-sectional SVD for dimensionality reduction and extraction of F_i magnitude. The F_i feature was combined with process parameters to predict the VB and RUL during face milling of Inconel 718. Furthermore, at every F_i threshold, the CNC machine was stopped to regulate the speed and feed based on the rapid rate of F_i evolution during machining. This process was iteratively explored to design the underlying cutting conditions that optimized the rate of F_i evolution at different wear levels during machining.

2.2 Description of the multi-sectional SVD and machine learning (ML) model

2.2.1 Dimensionality reduction by the multi-sectional SVD

Unlike the previous features extraction techniques, the multi-sectional SVD in this research extracted features from the region of interest (ROI), generated by the multi-sectioning algorithm, to demarcate the specific area that delineated the maximum VB level of 500 μm. Apart from the computational complexity, the ROI was found to be more effective in extracting the feature embeddings of the wear region than using the entire image [27]. In this case, the multi-sectioning algorithm was designed to locate the ROI slightly above the cutting edge to minimize the impact of the built-up edge (BUE) on the energy layers of the wear region. This was achieved by dividing the flank wear image into 160 sub-regions ($A1B1$, $A2B1$, …$A20B8$),

and then 40 sub-regions, which localized the ROI were selected. This resulted in a 75% reduction (from an area of 2,764,800 pixels to 691,200 pixels) in dimensionality even before latent features were extracted, thus, reducing the computational cost and time during MV-TCM application. The ROI was defined by 4 rows (B3–B6) and 10 columns (A3–A12).

Figure 3 illustrates the multi-sectional SVD approach for dimensionality reduction and feature extraction, depicting the decomposition of a high-dimensional tool wear image. The most informative features are extracted from the image matrix, streamlining the predictive modeling of tool wear evolution during machining. The figure demonstrates that each sub-region of the original wear image $AB \in \mathbb{R}^{m \times n}$ was then decomposed into three factors: U_{AB}, S_{AB}, and V_{AB}, as shown in (1) and (2), where $m = 180$ and $n = 96$. The matrix $S_{AB} \in \mathbb{R}^{r \times r}$ contained the singular values of the section AB, which represented the luminance layer of the wear region.
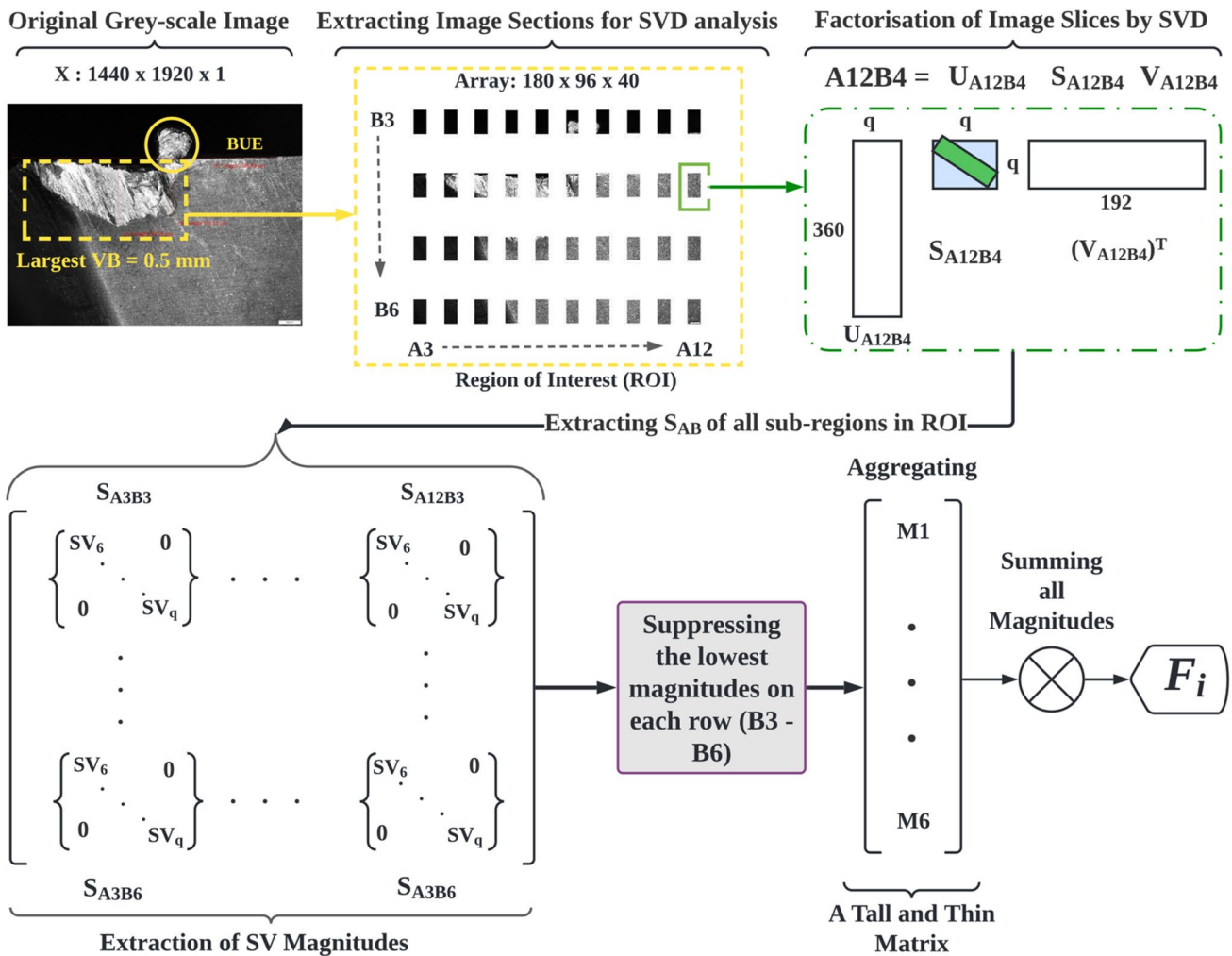

Fig. 3 The multi-sectional SVD approach for dimensionality reduction and feature extraction

The matrices $U_{AB} \in \mathbb{R}^{m \times r}$ and $V_{AB} \in \mathbb{R}^{r \times n}$ contained the left and right eigenvalues of the sub-region/section AB, respectively [20], where u_{ji} and v_{ji} were the left and right eigenvectors, respectively, and S_{AB} contained the singular values, $[\sigma_{11}, \sigma_{22} \dots \sigma_{rr}] = [\sqrt{\lambda_{11}}, \sqrt{\lambda_{22}} \dots \sqrt{\lambda_{rr}}]$, arranged in descending order (*Eqns.* (1) and (2)).

$$AB = U_{AB} S_{AB} V_{AB}{}^T \tag{1}$$

$$U_{AB} = \begin{bmatrix} u_{11} & \cdots & u_{r1} \\ \vdots & \ddots & \vdots \\ u_{1m} & \cdots & u_{rm} \end{bmatrix}; \ V_{AB} = \begin{bmatrix} v_{11} & \cdots & v_{1n} \\ \vdots & \ddots & \vdots \\ v_{r1} & \cdots & v_{rn} \end{bmatrix}; \ S_{AB} = \begin{bmatrix} \sqrt{\lambda_{11}} & \cdots & 0 \\ \vdots & \ddots & \vdots \\ 0 & \cdots & \sqrt{\lambda_{rr}} \end{bmatrix} = \begin{bmatrix} \sigma_{11} & \cdots & 0 \\ \vdots & \ddots & \vdots \\ 0 & \cdots & \sigma_{rr} \end{bmatrix} \tag{2}$$

2.2.2 Features extraction by the multi-sectional SVD

The singular values represented the strength of different energy layers in an image, as explained in [28]. As such, an *l2-norm*, derived from these singular values, was used to measure the magnitude of features in this research, also applied in other applications, as reported in [20]. *l2-norm* is mathematically equivalent to the largest singular values. After image decomposition, it was found that the first 5 singular values (SVs) had high *l2-norms*, which represented the highest luminous layers of the flank wear region during truncation, but they were not useful for identifying unique feature embeddings that distinguished progressive change in the flank wear depth (VB) during machining. Hence, these SVs were only used for image compression, but not to compute the SV magnitudes, as they stored invariant energy layers that were not capable of distinguishing the feature patterns that represented VB progression online. As a result, the time-varying features appeared at rank $q = 6$, where q is the effective rank for image compression out of the maximum rank r during truncation. The remaining $[r\text{-}q]$ *SVs* and their corresponding U_{AB} and V_{AB} matrices represented a noise component, which was eliminated in the process. Therefore, the magnitudes ($M(i, j)$) of singular values were calculated using the *l2-norm* of the S-diagonal vector (S_{AB}) by using Eq. (3) to represent the progressive change in the flank wear region.

$$M(i,j) = \sum_{r=1}^{q} \|S_{AiBj}\|_2 \tag{3}$$

The magnitude of singular values for the specific ranks ($M(i, j)$) was calculated for $i = 3\dots12$ and $j = 3\dots6$. From the rows ($B3$–$B6$), parallel to the main cutting edge, the maximum $M(i, j)$ values were selected by suppressing the sections with the lowest *l2-norms*. After aggregating these maximum $M(i, j)$s, the tall and thin column vector of the highest magnitudes was obtained. Figure 4 illustrates how the multi-sectional SVD separated the high-energy layer (HEL) sections from low energy layer (LEL) sections to retain the tall and column matrix representing the flank wear depth with the maximum magnitude of the basis vectors of U_{AB}. At this point, the significance of the unprecedented failure modes, localized on the wear region, was reduced as the HELs originated from the ROIs free from chipping, notching, flaking,
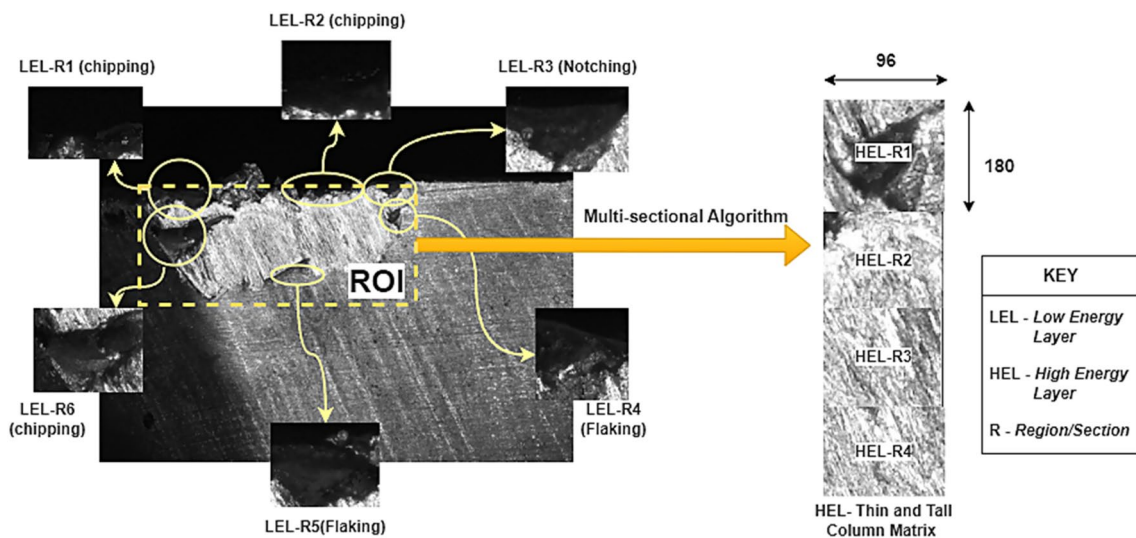

Fig. 4 The multi-sectional SVD for dimensionality reduction and extraction of the highest energy layer along the flank wear depth

and BUE (regions of LELs). This feature matrix was then used to compute the final feature (F_i), which represented the highest energy layer of the entire flank wear depth, as illustrated in Fig. 3. By doing so, the method reduced the noise attributed to the unprecedented failure modes, thus overcoming the multi-modal effect of smeared images during features extraction. This method was validated by correlating the extracted F_i feature with the actual VB at various process conditions.

2.2.3 Evaluating the performance of multi-sectional SVD

The performance of the multi-sectional SVD was evaluated using compression ratio (R) (4), peak signal-to-noise ratio ($PSNR$) (5), mean square error (MSE) (6), and structural similarity index measure ($SSIM$) (8), as described in [20, 21]. The compression ratio quantified the percentage reduction of the sub-regions during truncation. Upon decomposition, if the rank q was equal to the width of the image (n), then the dimensions of matrix U_{AB} were congruent to those of AB, while if q was equal to the height of the image (m), then the dimensions of matrix V_{AB} were equivalent to those of AB. Hence, the image was only compressed if q was less than m or n. On the other hand, the $PSNR$ served as a logarithmic gauge of the quality of a reconstructed image following compression, thus guaranteeing that the predominant features were fully reinstated within the wear region. The $PSNR$ was calculated based on the MSE between the original AB and the reconstructed image section AB'. It was observed that the values of R, SNR, and $PSNR$ estimated the error in image reconstruction, while $SSIM$ validates the SVD's ability to recreate the structural interdependence of pixel distribution and energy layers between the original image AB and the truncated image AB'. $SSIM$ is calculated using small windows of 11×11 (window ab for AB and ab' for AB') pixels, where a value close to 1 indicated a high structural similarity of the original and truncated image. The $SSIM$ performance of the multi-sectional SVD was evaluated using 3 structural components namely, luminance (l), contrast (c), and structure (s), as shown in (8). Combining all equations in (7) gives (8) [20].

$$R = \frac{(nq + q + mq)}{mn} \times 100\% \tag{4}$$

$$PSNR\,(dB) = 20log_{10}\left(\frac{MAX_{AB}}{\sqrt{MSE}}\right) \tag{5}$$

$$MSE = \frac{1}{mn}\sum_{i=1}^{n}\sum_{j=1}^{m}\left[AB(i,j) - AB'(i,j)\right]^2 \tag{6}$$

$$l_{(ab,ab')} = \frac{2\mu_{ab}\mu_{ab'}+q_1}{\mu_{ab}^2+\mu_{ab'}^2+q_1};\ c_{(a,g)} = \frac{2\sigma_{ab}\sigma_{ab'}+q_2}{\sigma_{ab}^2+\sigma_{ab'}^2+q_2};\ s_{(ab,ab')} = \frac{\sigma_{ab,ab'}+q_3}{\sigma_{ab}\sigma_{ab'}+q_3} \tag{7}$$

$$q_1 = (a_1b)^2\ \ q_2 = (a_2b)^2\ \ q_3 = \frac{q_2}{2}$$
$$SSIM_{(ab,ab')} = \frac{(2\mu_{ab}\mu_{ab'}+q_1)(2\sigma_{ab,ab'}+q_2)}{(\mu_{ab}^2+\mu_{ab'}^2+q_1)(\sigma_{ab}^2+\sigma_{ab'}^2+q_2)} \tag{8}$$

where q is the final rank of truncating AB'; MAX_{AB} is the maximum pixel value of AB; μ_{ab} and μ_{ab} are the mean value of windows ab and ab'; σ_{ab}, $\sigma_{ab'}$, and $\sigma_{ab,ab}$ are standard deviations and covariance of windows ab and ab', respectively; q_1, q_2, and q_3 is a luminance, contrast, and structure constants; b is the dynamic range of pixels represented by ($2^{bitsperpixel} - 1$); and $a_1 = 0.01$ and $a_2 = 0.03$ (default values when evaluating $SSIM$). The multi-sectioning algorithm is summarized in Algorithm 1.

Algorithm 1 Multi-section SVD

```
1:  compressionratio(r) ← m * n/(r * (m + n + 1))
2:  function Loop([ ])
3:      X(:,:,1) ← inputimage
4:      [AB] ← X(:,:,1 : 160)
5:      Rank_max ← 5 : 60
6:      [U_AB(:,:,e), S_AB(:,:,e), V_AB(:,:,e)'] ← svd(AB(:,:,e))
7:      for e ← 0 to Rank_max do
8:          [ca(:,:,e)] ← deal(U_AB(:,1 : q,e) * S_AB(1 : q,1 : q,e) * V_AB(1 : q,:,e)')
9:          RMSE(q,e) ← √((AB(:,:,e) - ca(:,:,e))²)
10:         [PSNR] ← psnr(ca(:,:,e), AB(:,:,e))
11:         [SSIMval(q,e), SSIMmap(q,e)] ← ssim(ca(:,:,e), AB(:,:,e));
12:         [σ_AB] ← S(q+1,e)
13:     return [M(i,j)] ← norm(λ(:,:,e))
14:     return [F_i] ← ∑ M(i,j)
```

2.2.4 Training the ML model

In order to demonstrate the real application of the multi-sectional SVD during MV-TCM, F_i features were combined with process parameters to train an ML model (ANN in MATLAB R2019b), for the purpose of predicting VB and RUL progression during face milling of Inconel 718. Then, the standard score was applied to normalize the feature predictive strength before training the ML model. The ML applied a Levenberg–Marquardt algorithm (LMA), and the performance was measured using the mean squared error (MSE) loss function [29]. The backpropagation (10) was used to compute the partial derivative (9) to minimize the loss function. A purelin transfer function (f) was used because the model applied regression analysis to compute the VB and RUL values. Considering that the VB and RUL
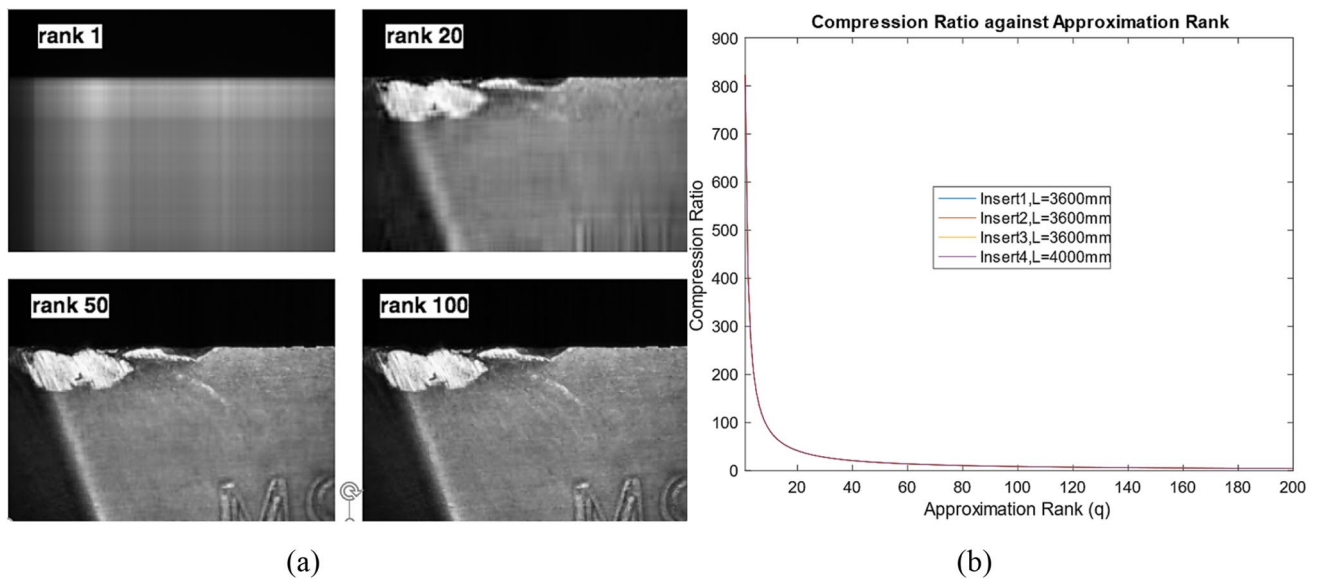
(a)

(b)

Fig. 5 **a** Image truncation with varying ranks at $V_c = 40$ m/min, $f_t = 0.07$ mm/tooth, $a_p = 1$ mm, and L = 4400 mm and **b** compression ratio

were significantly affected by the cutting speed, feed rate, depth of cut, and F_i feature, the ML architecture had 4 neurons in the input layer (corresponding to the 4 inputs) and 2 neurons in the output layer (corresponding the 2 outputs, which are VB and RUL). The optimal number of neurons in the hidden layer was determined manually during training.

$$MSE = \frac{1}{n} \sum_{i=1}^{n} \left(VB_t - VB_y \right)^2 = \frac{1}{n} \sum_{i=1}^{n} (\epsilon)^2;$$

$$(b) y_j = f\left(b + \sum_{k=1}^{N} w_{kj} - x_k \right) \tag{9}$$

$$\frac{d\epsilon}{dw_{kj}} = \frac{d\epsilon}{dy_j} \frac{dy_j}{dw_{kj}} = \frac{d\epsilon}{y_j} \cdot \frac{dy_j}{d\left(\sum_{k=1}^{N} w_{kj} - x_k \right)} \cdot \frac{d\left(\sum_{k=1}^{N} w_{kj} - x_k \right)}{dw_{kj}} \tag{10}$$

where x_k is the input to a neuron, ε is the error, w_{kj} is the weight between neuron k of previous layer and j of the current layer, y_j is the output of j neuron, VB_t is the target flank wear, and VB_y is the predicted output. After training the ML model, it was integrated with the multi-sectional SVD architecture and MV-TCM system to extract F_i features and predict RUL online during face milling of Inconel 718. At this point, the rate of F_i and RUL evolution was evaluated at different wear stages to determine the promising speed and feed that minimized the wear rate during machining, thereby designing the optimal cutting condition that improved the performance of the PVD-TiAlN/NbN-coated carbide inserts during face milling of Inconel 718.

3 Results and discussion

3.1 Performance of multi-sectional SVD

The results showed that the multi-sectional SVD successfully reduced the dimensions of tool wear images, denoised the wear region, extracted, and selected reliable features that augmented process parameters to predict the rate of VB and RUL online, regardless of variations in the image resolution and cutting conditions during face milling of Inconel 718. Figure 5 shows the effects of image truncation at different ranks under specific machining conditions. As the rank decreases, representing a lower-dimensional approximation of the original tool wear image, the compression ratio increases, indicating greater data compression achieved through truncation while retaining essential image structure and information. Figure 5 a shows image truncation at various ranks.

The results showed that at the first 5 ranks, the image features were not clear enough to distinguish the worn from the unworn part of the tool. Thus, the first 5 singular values were responsible for capturing the highest energy layers of the flank wear images. However, above rank 6, the clarity improved, and there were small discrepancies between the original and reduced-rank image. In addition, the analysis of the average relative norm, RMSE, SNR, and PSNR indicated the steady rate in signal evolution and image restoration after rank 50, as depicted in Fig. 6a, b, c, and d, indicating noise reduction during truncation. Figure 6 shows the performance metrics of the multi-sectional SVD, highlighting its effectiveness through various indicators, such as (a) relative-2 norm, (b) root mean square error (RMSE), (c)
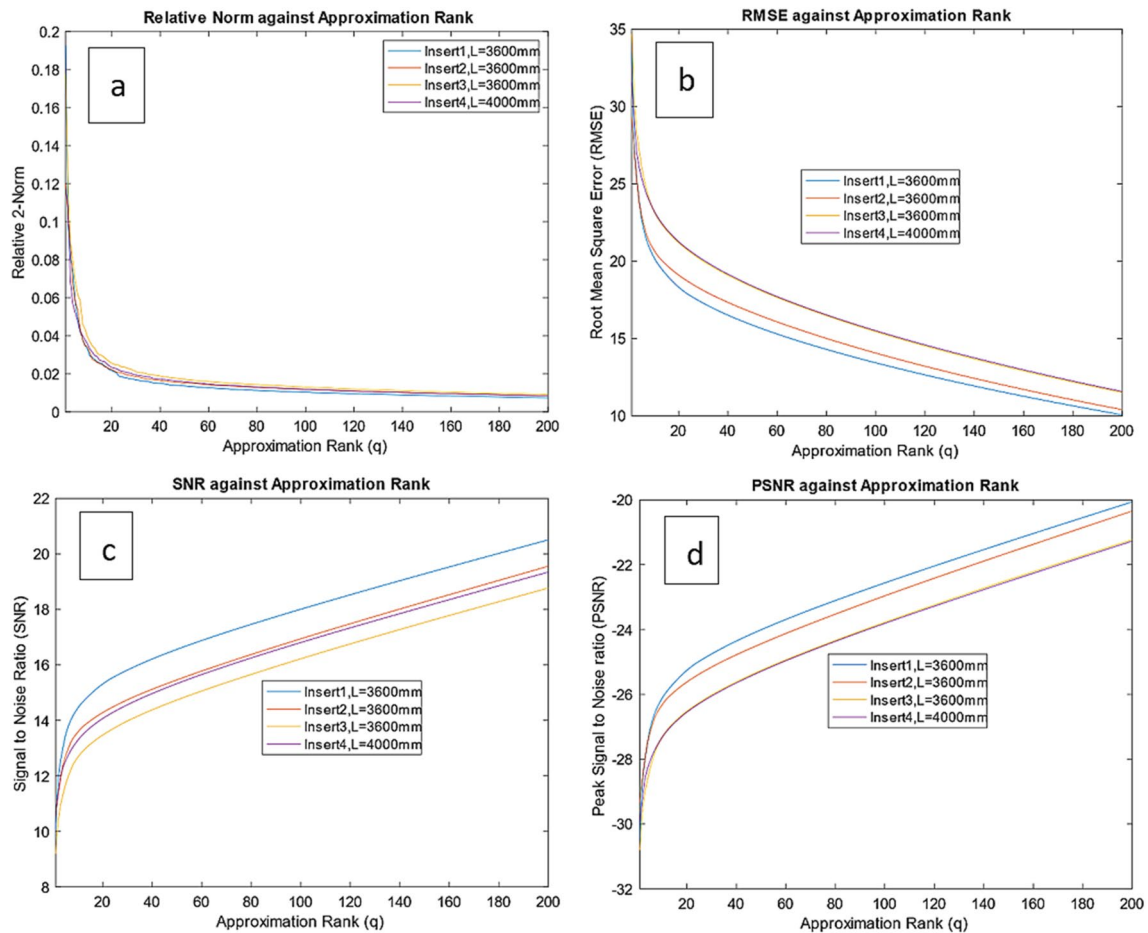
Fig. 6 Multi-sectional SVD performance curves during image truncation: **a** Relative-2 norm, **b** RMSE, **c** SNR, and **d** PSNR

signal-to-noise ratio (SNR), and (d) peak signal-to-noise ratio (PSNR). Each metric provides insights into the characteristics of the decomposed tool wear images, highlighting the capability of the Multi-sectional SVD in preserving significant features while minimizing noise during truncation. Thus, the significant image information was fully restored at rank 60, and increasing the rank had no significant effect on the image quality and could even reintroduce noise on the wear region. As a result, middle SV values ($5 < q < 60$) were used when computing the F_i features. The remaining (r-q) singular values were used to reconstruct the noise component.

3.1.1 Cutting speed

After extracting the F_i features from time-series flank wear images, they were correlated with process parameters to design a promising cutting condition and feature thresholds for in-process utilization during MV-TCM. Figure 7 illustrates the correlation of Fi magnitudes with four key machining parameters: (a) cutting speed, (b) feed rate, (c) depth of cut,

and (d) measured VB (flank wear). Each subplot shows the relationship between the magnitude of Fi, which provides valuable insights into the variations of these parameters and complex tool wear evolution during face milling of Inconel 718. The magnitudes of F_i were strongly correlated with the cutting speed, as shown in Fig. 7a. At a cutting speed of 80 m/min, the high rate of friction and abrasion accelerated the progressive change in energy layers on the tool's cutting edge, resulting in the rapid evolution of the F_i magnitudes towards the critical and failure region. In this case, the F_i features failed to exhibit a steady wear phase. On the other hand, at cutting speeds of 40 and 60 m/min, the F_i magnitudes displayed a uniform wear region. This wear phenomenon was attributed to the reduced cutting temperature, which minimized the friction and abrasion wear mechanisms, thereby maintaining the slow evolution of the energy layers in the uniform flank wear region. The trend of F_i progression at 40 m/min was consistent with the actual VB profile obtained in [15], indicating a high correlation between the F_i magnitudes and actual VB progression for the lowest cutting speed. At 60 m/min, there was a rapid rate of F_i progression, which was attributed to the
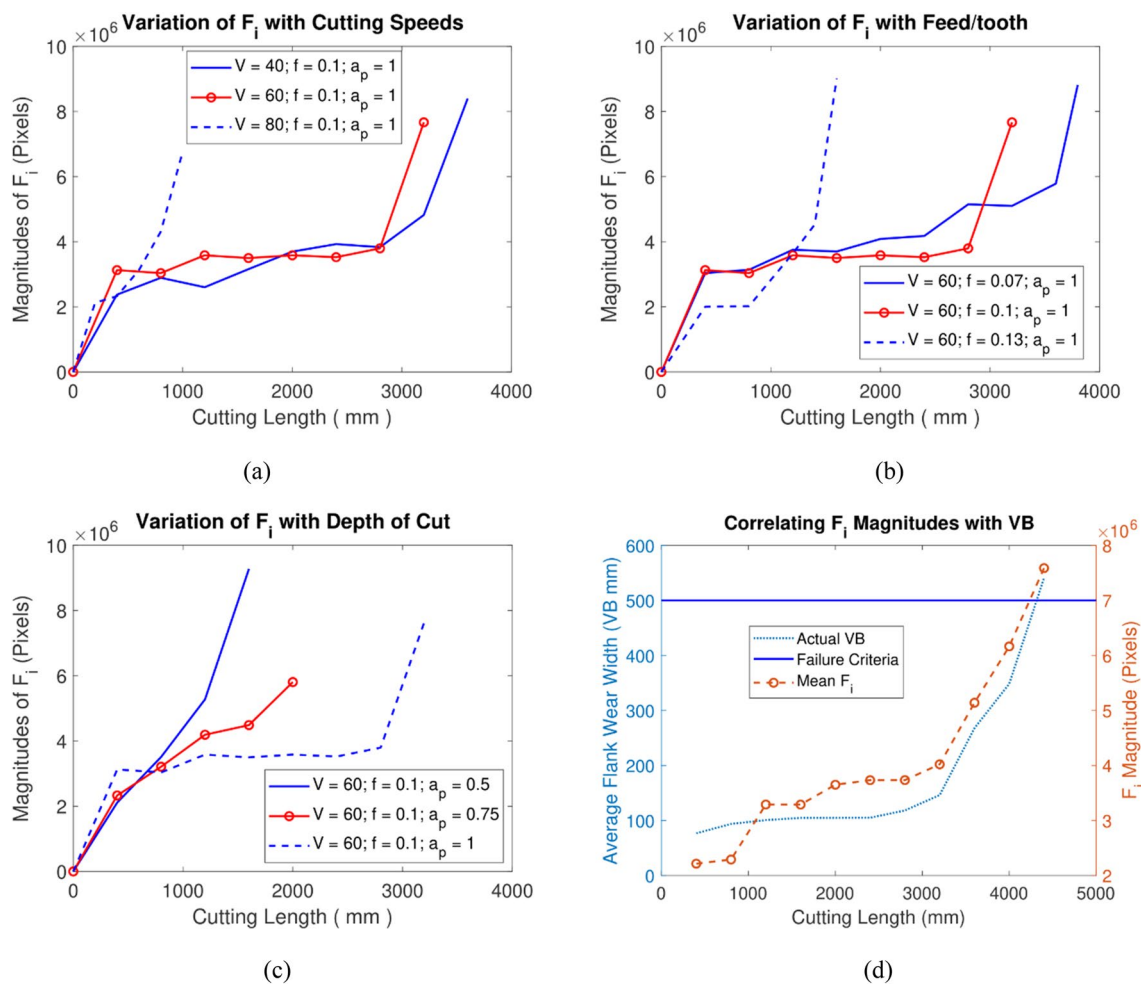
Fig. 7 Correlation of F$_i$ magnitudes with **a** cutting speed; **b** feed rate; **c** depth of cut; and **d** measured VB

intermittent evolution of energy layers in some sections of the flank wear region due to cyclic BUE and chipping formation. This eventually caused inconsistent and fluctuating evolution of the energy layers and F_i magnitudes, resulting in a shorter cutting length and tool life as compared to the lowest cutting speed of 40 m/min.

3.1.2 Feed/tooth

The magnitudes of F_i also correlated with the feed per tooth, as depicted in Fig. 7b. At 0.13 mm/tooth, the formation of built-up edge (BUE) was attributed to the largest chip load, which led to progressive chipping under moderate abrasion at medium speed of 60 m/min. This caused the F_i magnitudes to fluctuate towards the critical and failure regions, resulting in an unpredictable trend that cannot accurately extrapolate the VB profile. At 0.1 mm/tooth, the F_i progressed uniformly, owing to the consistent evolution of the energy layers at the flank wear region due to less chipping and BUE formation at a medium speed. At the lowest feed

rate of 0.07 mm/tooth, the reduced chip load resulted in a rubbing action between the tool and workpiece, generating more friction and abrasion wear mechanism, especially at a medium speed of 60 m/min. This led to higher energy layers as compared to 0.1 mm/tooth, which progressed consistently to generate the uniform evolution of F_i magnitude. Therefore, the progressive trend of F_i magnitudes at the lowest feed/tooth was in accordance with the VB curve obtained in [15], indicating high predictive efficiency for a uniform VB rate during face milling of Inconel 718.

3.1.3 Depth of cut

Furthermore, the magnitudes of F_i were correlated with the ADOC, as shown in Fig. 7c. It was observed that at 0.5 mm ADOC, F_i progressed exponentially due to severe chipping at the DOC line, as the effective cutting edge was used to remove the precipitation hardened layer of Inconel 718. At a 0.75 mm ADOC, the cutting edge still experienced progressive chipping at the DOC line, but at a slower rate

Table 5 Thresholds of VB and F_i magnitudes for determining the failure criteria

Levels	LTV_{early}	$LTVUniform$	$LTV_{critical}$	$LTVFailure$
VB (μm)	100	200	300	500
F_i (Pixels)	2,000,000	4,000,000	5,000,000	7,000,000

as compared to 0.5 mm due to the reduced impact of the precipitation-hardening at slightly larger ADOC. At 1 mm, the magnitudes of F_i evolved uniformly due to lower chipping magnitudes as most of the cutting edge was used to cut the subjacent layers of the workpiece material, free from the precipitation hardening effect. Additionally, the synergistic effect of the largest ADOC, medium feed, and speed increased the chip load and friction, generating high-energy layers that stabilized the evolution of F_i magnitudes in the uniform wear stage. Therefore, the results of F_i evolution at the largest ADOC agreed with the VB curve in [15].

3.1.4 Lowest speed and feed

In summary, the evolution of the F_i magnitudes was a strong predictor variable of the flank wear depth at the lowest speed of 40 m/min, lowest feed of 0.07 mm/tooth, and largest ADOC of 1 mm. Therefore, the mean values of F_i magnitudes were plotted together with the measured VB at this cutting condition, as shown in Fig. 7d. The results showed that F_i values ranged between 2,000,000 and 7,000,000 pixels for all flank wear levels, including early, uniform, critical, and failure stages, with 7,000,000 corresponding to the maximum failure criteria of $VB = 500$ μm. This multicollinear correlation was used to establish F_i thresholds at various flank wear levels, as shown in Table 5. It is also worth noting that the F_i magnitudes were strong predictors of the flank wear evolution in the early and uniform wear region, where the impact of the synergistic wear mechanisms was insignificant. However, the unprecedented failure modes, which exacerbated the loss in energy layers for some sections of the wear region, especially in the critical and failure stages, fluctuates the F_i feature, making it unstable to predict flank wear depth during machining.

3.2 Performance of ML using multi-sectional SVD features

From the analysis above, it is evident that the F_i feature strongly correlated with flank wear depth; thus, it can be used as a predictor variable of VB and RUL evolution in addition to the process parameters. This means there were 4 predictor variables of VB and RUL. However, in cases where the input parameters are fixed during the machining process, the F_i feature becomes the only indicator of tool wear evolution, making it more significant for online VB and RUL prediction during MV-TCM as most machining industries operate under fixed cutting conditions. To further substantiate the effectiveness of the multi-sectional SVD, a machine learning model (ANN) was trained with input features of speed, feed, axial depth of cut, and F_i magnitude to predict the progressive VB and RUL of the tools during face milling of Inconel 718. When developing an ML, training data was further split into 80% training, 10% validation, and 10% testing within the learning process. The learning rate of the model was set at 0.0001. After evaluating the training performance, the architecture with 8 neurons in the hidden layer showed the best performance at epochs 16, with a validation MSE of 0.17479 mm, as shown in Fig. 8, relative to the weights and biases in Table 6. Each plot of Fig. 8 shows the mean square error metric across different stages of model training, validation, and testing, indicating how well the model generalizes to the unknown conditions, thus providing insights into its ability to effectively learn from the training data and make accurate predictions on new data. After evaluating the individual performances, the *VB* and *RUL* errors were distributed between -0.3331 to 0.4275 μm and -0.2245 to 0.1195 μm, respectively, with the highest instances at -0.01288 μm and -0.00728 min close to the zero-error line. Figure 9 shows histograms of the machine learning model for both (a) VB (flank wear) and (b) RUL (remaining useful life) predictions. The subplots depict error distribution between the predicted and actual VB and RUL values, respectively, providing insights into the accuracy and precision of the model across different prediction tasks.

Furthermore, Fig. 10 evaluates the relationship between the predicted values and the actual measurements, providing insights into the model's predictive accuracy and its ability to estimate VB and RUL effectively, thereby understanding the model's performance across the predictions of different conditions and allowing for the examination of any potential biases or trends in the predictions. The ANN-regression coefficient of 0.98053 in Fig. 10a and 0.99927 in Fig. 10b confirms the highest correlation of the predicted against actual VB and RUL, respectively. This phenomenon was attributed to uniform flank wear or microchipping, which barely affected the energy layers on the flank wear region in the early cutting stages. However, near the failure region, the tools experienced severe chipping and BUE (built-up edge), which distorted the pixel distribution, reducing the wear region's energy layers and F_i magnitudes. In addition, the chipping or flaking exposed the tool substrate, disrupting the pixel distribution and evolution of the F_i magnitudes.

After training the ML model, it was validated using the test dataset, which was obtained from a cutting condition outside the vicinity of the training process parameters. Figure 11 demonstrates the validation of machine learning (ML)

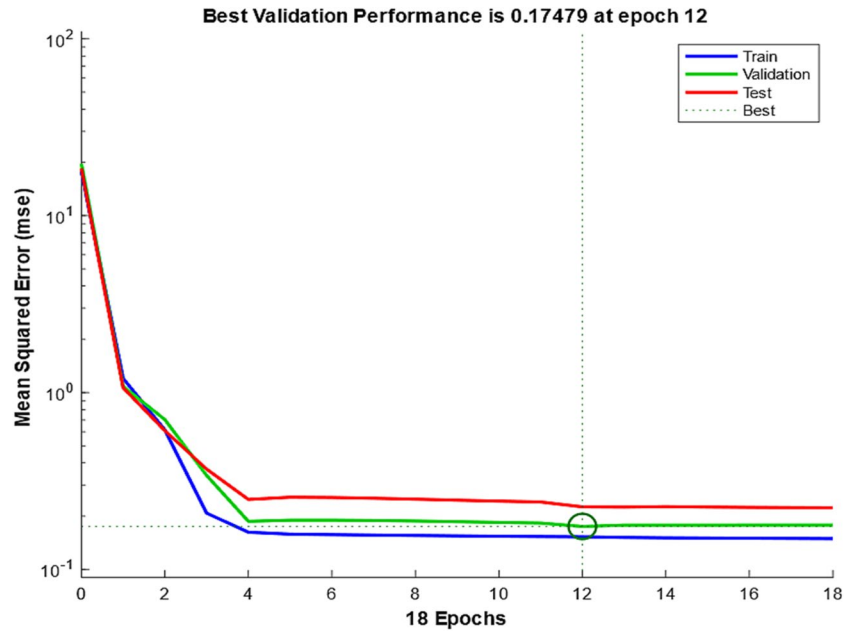**Fig. 8** Training, validation, and test performance curves of the ML model

Table 6 Parameters of the ML model [IW1, B1– weight and bias for layer 1; OW– output layer weight]

IW1	1W2	1W3	1W4	OW1	OW1	B1	B2
2.667	−0.888	0.980	3.152	0.42	0.077	3.526	−0.002
4.637	3.009	−0.160	1.355	0.17	0.0621	−2.112	−0.370
−2317	−0.379	−1.807	−1.804	−0.84	−0.094	−1.017	
−1.344	−0.268	−0.145	−1.599	0.04	−0.345	0.336	
−3.689	−2.400	0.590	−1.063	0.10	2.321	1.819	
−0.685	1.280	1.046	−1.324	−0.16	−0.342	−0.380	
−0.444	0.091	0.225	−0.542	0.55	1.281	−0.246	
1.163	4348	1.703	−1.013	−0.176	−0.467	−2.438	
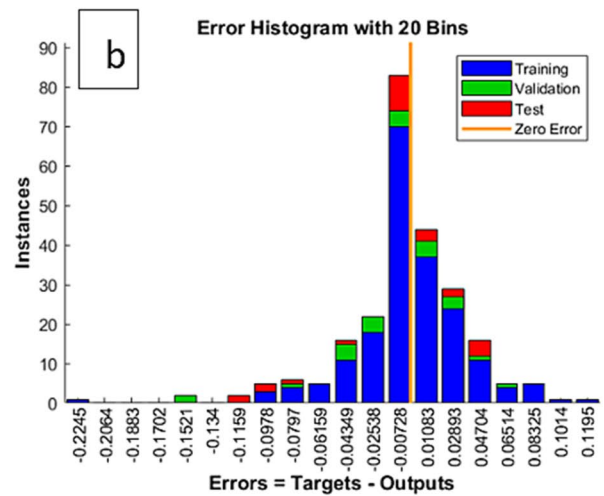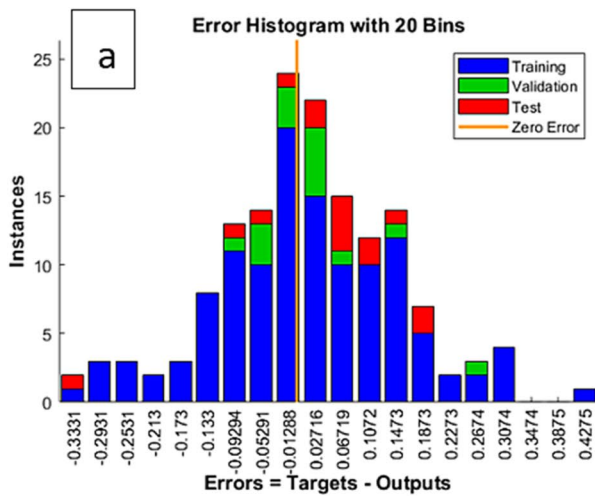
Fig. 9 Error histograms of the ML **a** VB and **b** RUL
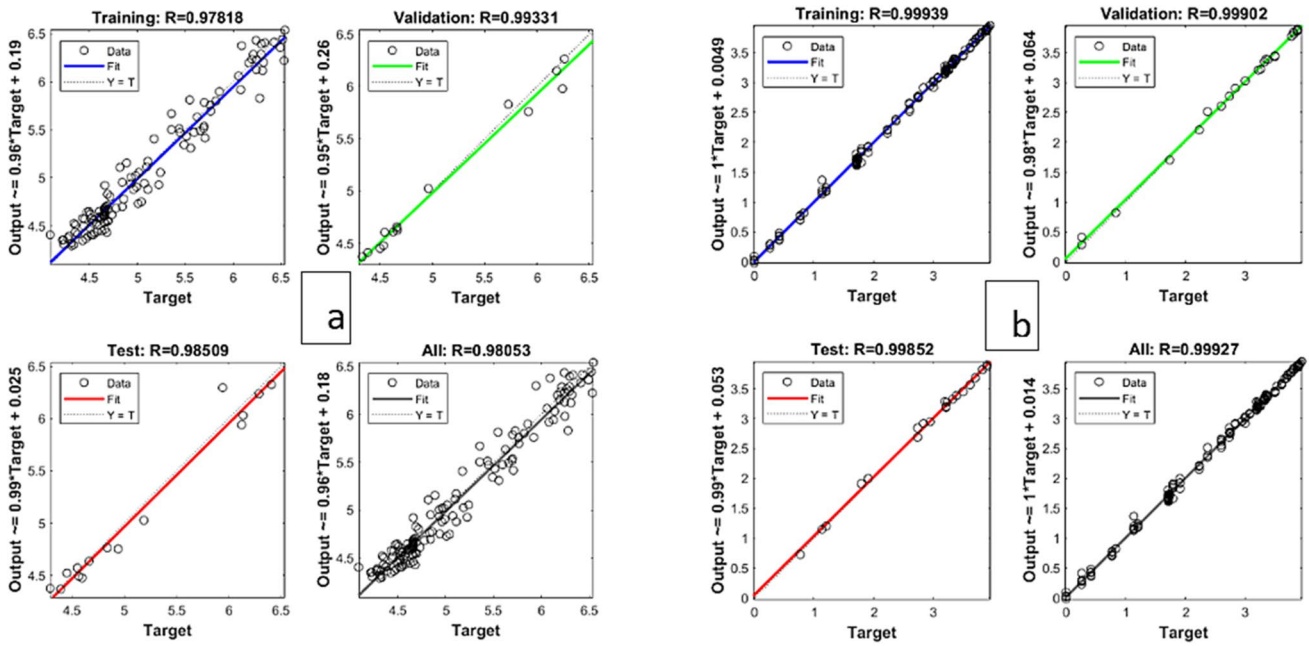
Fig. 10 The regression analysis of the ML **a** VB and **b** RUL
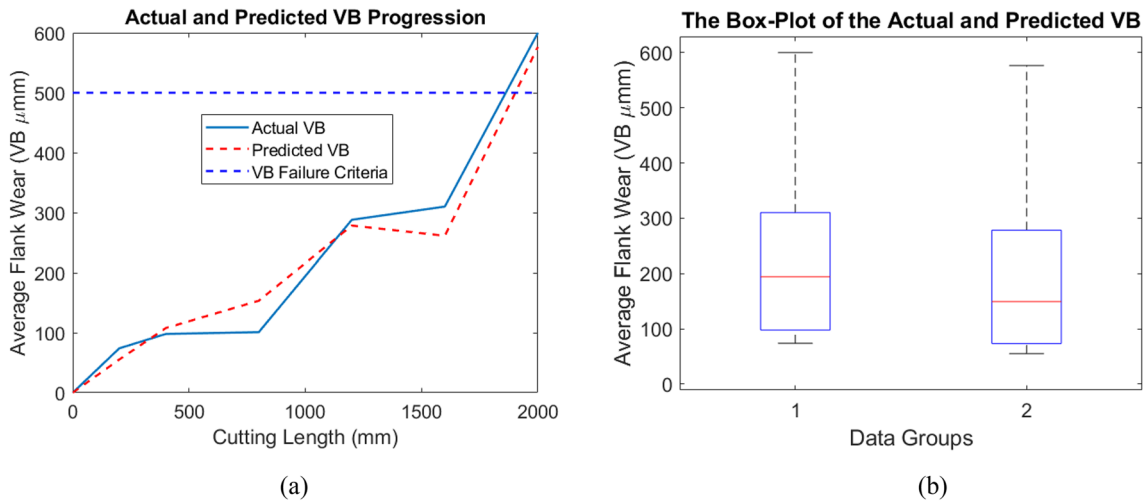

Fig. 11 a Validation of ML performance for VB prediction using test data, **b** boxplot for actual and predicted VB

performance for VB prediction using test data, where the boxplot compares the distribution of actual and predicted VB, thereby providing accuracy and variability of the model's predictions. Figure 11b shows the boxplot for VB during testing. The median skewed towards small values less than 200 μm, indicating high prediction accuracy for small VB values. The results showed that the mean predicted VB (data2) had a small deviation of 45.5 μm with measured values. It yielded a mean absolute error of 2.36%, which is lower than the values obtained in previous studies [30] and [31], where only geometric features were used to predict

VB progression during machining. Additionally, the boxplot indicates that there were no outliers, which means the predicted data strongly fitted within the expected range of measured values. The substantial decrease in predicted VB near the critical and failure regions, as shown in Fig. 11a, was attributed to the severe chipping, notching, flaking, and catastrophic failure of the tool cutting edge when milling Inconel 718. Furthermore, Fig. 12 illustrates the validation of machine learning (ML), which is depicted through an RUL curve, providing the insights into the accuracy and precision of the model's predictions over the entire range

of RUL. Figure 12b illustrates the boxplot of RUL during testing, with a median difference of −5.3 min, indicating that the predicted values were slightly higher than the actual RUL values, which is a normal case for ANN models as they cannot produce a zero-output value during regression analysis. The plot shows that there was no substantial difference between actual (data1) and predicted RUL (data2). Additionally, the RUL boxplot had no outliers, which means the ML model predicted multicollinear data that perfectly fitted within the expected range of the measured values.

However, it was noted that the substantial reduction in RUL at the early cutting stage was attributed to the severe BUE (built-up edge) due to a large chip load at the highest feed of 0.13 mm/tooth. Figure 13 visualizes how different failure modes change over the course of cutting operations and varying cutting lengths, facilitating the understanding of the impact of cutting parameters on tool wear behavior and optimization of the machining processes for improved tool life extension. After subsequent passes, the BUE was removed by continuous chip flow, resulting in notching and chipping on the tool cutting edge, as shown in Fig. 13c and d. Such unprecedented failure modes increased the wear rate and RUL, making the models unable to achieve the expected value of 0 min at the end of tool life. This is why Fig. 12a shows that the RUL of the tools was 1.7 min at a maximum cutting length of 2000 mm. Furthermore, the median of the predicted RUL was skewed towards larger values, indicating a shorter RUL in the failure region as compared to the actual measurements. This was attributed to the rapid failure of the tools in the critical and failure wear stages. Nevertheless, the ML model still yielded a high performance, with a MAPE of 3.078%, indicating a high correlation between actual and predicted RUL.

3.3 In-process control of F_i feature

After training and validating the multi-sectional SVD-based ML model for tool wear prediction, it was applied for optimizing the tool life by adjusting the cutting parameters to minimize the rate of F_i and RUL during the machining process. At this point, due to high correlation between F_i and VB, it was believed that the F_i feature was a direct predictor and indicator of tool wear evolution. This means minimizing this feature was as good as minimizing the VB progression during face milling of Inconel 718. According to the experimental findings in [2] and [15], the uniform flank wear evolution, whose magnitude was detected by F_i feature was the most preferred failure mode during face milling of Inconel 718. For this reason, the severe abrasion wear, which is the main causative mechanism of the non-uniform flank wear progression [32], was supposed to be minimized to reduce the rapid evolution of the unprecedented failure modes, and improve the rate of RUL. In this case, the lowest speed below 40 m/min reduced the cutting temperature and severe abrasion wear mechanism, which in the long run reduces the macro-chipping during machining. On the other hand, the feed rate below 0.08 mm/tooth reduced the cyclic adhesion and BUE due to moderate chip load [33], especially in the critical and failure wear stages, resulting in the low rate of F_i evolution as no significant BUE got removed together with the aggressive chip flow. In addition, the ADOC greater than 0.9 mm reduced the localized chipping in the depth of cut (DOC) region, making the tools survive more impact forces at the lowest speed and feed/tooth. However, the ADOC had less impact on F_i evolution as compared to the speed and feed/tooth; as a result, it was kept constant during the optimization process.
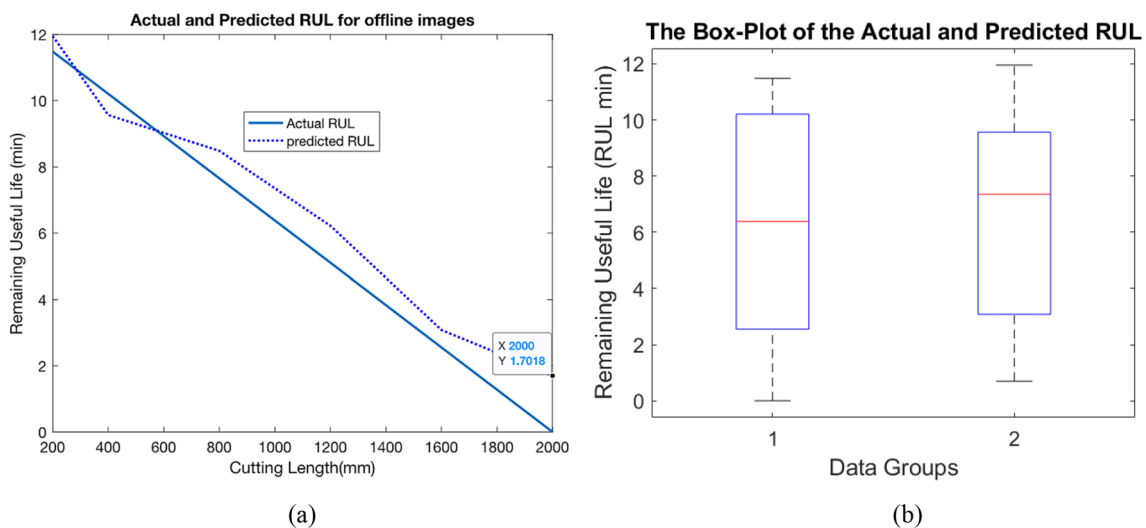

(a)　　　　(b)

Fig. 12 Validation of ML performance for RUL prediction using test data: **a** RUL curve and **b** boxplot of RUL
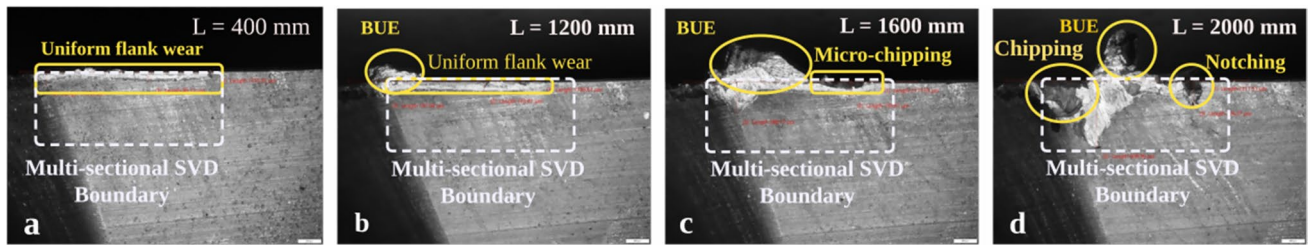
Fig. 13 Evolution of failure modes with cutting length (L) at $V_c = 40$ m/min, $f = 0.13$ mm/tooth, and $a_p = 1$ mm
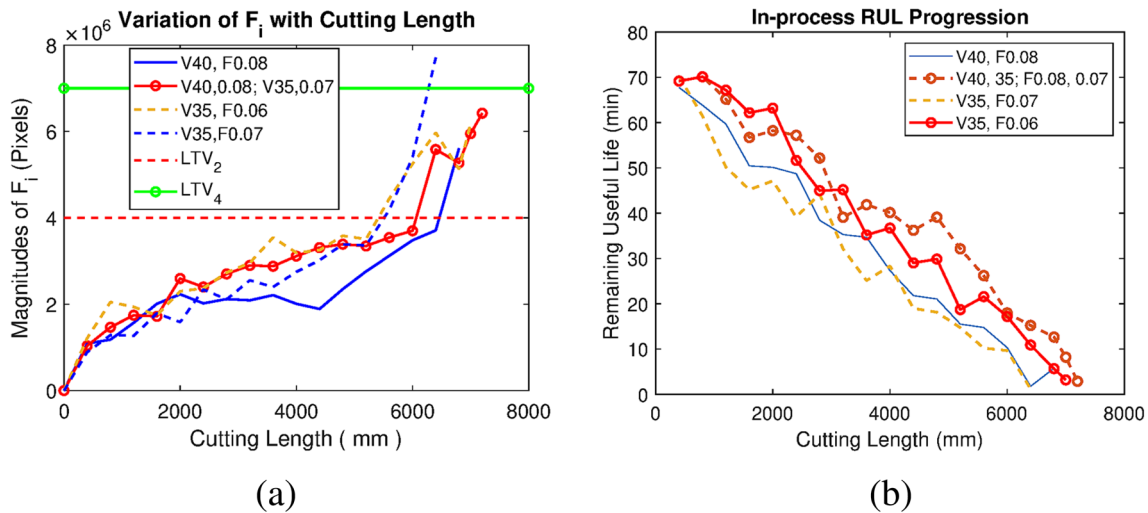

Fig. 14 **a** Evolution of F_i magnitudes and **b** the RUL profiles at various speeds and feeds

Therefore, the cutting speed of 35 and 40 m/min, and feed rate of 0.06, 0.07, and 0.08 mm/tooth was significant levels of speed and feed, whose synergy was believed to extend tool life, according to the findings presented in [6].

Figure 14 presents the evolution of Fi magnitudes and RUL profiles at varying speeds and feeds. The figure provides insights into the effects of these parameters on tool life extension, thereby offering an understanding of the dynamic behavior of tool wear evolution under varying processing conditions. The speed and feed adjustment were first performed at a speed of 40 m/min, feed of 0.08 mm/tooth, and ADOC of 0.9 mm, which was the initial optimal condition designed by the GKRR model in [6]. It was perceived that the tools sustained a moderate temperature, friction, and chip load, which were attributed to the moderate adhesion wear mechanism on the tool's cutting edge. The moderate chip load and speed resulted in high friction and plastic deformation, which exacerbated the asperities deformation in the early cutting stages, producing a protective layer superjacent to the TiAlN/NbN coating [33]. This layer prevented the tool's coating or substrate from further degradation or chipping by severe abrasion wear mechanism in the subsequent passes of the machining process. As a result, tools at

this condition experienced the lowest F_i magnitudes in the uniform wear region, as shown in Fig. 14a. However, the moderate chip load at 0.08 mm/tooth feed rate exacerbated the cyclic adhesion and abrasion, which resulted in severe chipping in the critical and failure regions, thus reducing the rate of RUL (Fig. 14b).

After randomly reducing the speed from 40 to 35 m/min, and feed from 0.08 to 0.07 mm/tooth, the tools experienced low friction, galling, and asperities deformation due to low temperature and reduced chip load on the tool's cutting edge. This reduced the BUE, thereby preventing the formation of the protective layer superjacent to the TiAlN/NbN coating, making the rate of tool degradation faster as compared to the 40 m/min and 0.08 mm/tooth. The same had the maximum rate of RUL in all the cutting stages (Fig. 14b). Although this wear phenomenon minimized the evolution of the chipping magnitudes in the critical and failure wear stages, the absence of the protective layer hastened the rate of F_i and RUL progression due to abrasion wear mechanism, especially in the early cutting stages. By further decreasing the feed rate to 0.06 mm/tooth, the detrimental effects of intense friction and rubbing action further reduced the chipping rate in the early cutting stages. Contrary, such wear phenomenon also increased the energy layers on the

wear region, leading to high F_i and RUL evolution. Nevertheless, it reduced the impact of the cyclic adhesion and severe abrasion wear mechanisms, which, in the long run, minimized the progressive chipping in the critical wear stage as no BUE was plucked together with chip flow. This yielded a longer cutting length in the critical and failure regions as compared to the previous condition of $V_c = 40$ m/min and $f_t = 0.08$ mm/tooth.

Therefore, 40 m/min and 0.08 mm/tooth yielded a better performance in the early cutting stages, whereas 35 m/min and 0.07 mm/tooth yielded a better performance in the critical and failure stages. Thus, the combination of moderate VB rate in the critical and failure wear phases at a cutting speed of 35 m/min and a feed rate of 0.07 mm/tooth was successfully integrated with the effectiveness of F_i evolution achieved at 40 m/min and 0.08 mm/tooth in reducing the rate of RUL, particularly in the early cutting phases. As previously noted, the former helped to minimize cyclic adhesion, thereby reducing the impact of chipping progression in critical and failure regions, whereas the latter introduced the protective layer superjacent to the TiAlN/NbN coating, which prevented the premature tool failure, especially in the early cutting stages, when face milling Inconel 718. Therefore, a multi-stage adjustment of speed and feed rate at different wear stages was found to be more effective in minimizing the rate of F_i and RUL evolution as compared to a one-time adjustment of the processing conditions.

4 Conclusion

This research shows the potential of a multi-sectional SVD-based ML in dimensionality reduction, feature extraction form time-series tool wear signals, and prediction of progressive VB and RUL during face milling of Inconel 718. The magnitudes of singular values (F_i features) had a strong correlation with the flank wear depth at various processing conditions. Unlike the previous models, the proposed multi-sectional SVD-based ML was effective in predicting VB and RUL under limited dataset during MV-TCM. The ML model showed high prediction accuracy at early cutting stages, where the tools experienced less discrepancies on the evolution of energy layers due to minimum occurrence of the unprecedented failure modes and wear mechanisms. However, the prediction accuracy decreased near the critical and failure stages due to severe chipping and BUE formation, which distorted the wear region's pixel distribution and energy layers, resulting in low SV magnitudes and inconsistent rate of the F_i, VB, and RUL features on the flank wear region. It was also observed that the energy layers and Fi magnitudes fluctuated under unstable lighting conditions; thus, a good MV-TCM set-up should ensure consistent lighting conditions to yield enhanced resolution of tool wear images before features extraction. Nevertheless, the multi-sectional SVD-based ML yielded the high performance, with a MAPE of 2.36% and 3.078% for VB and RUL, respectively.

The model was further applied to design the promising cutting condition, where it was revealed that the multi-stage adjustment of speed and feed can improve the tool performance during face milling of Inconel 718. It was believed that the system's performance can be improved through the utilization of the multi-plex MV-TCM cameras, stacked auto-encoders and deep learning architectures, which provide complex computing techniques to improve the feature engineering process.

The research offers some proven evidence of advances in the field of MV-TCM. The methodology of this research demonstrated model's effectiveness in dimensionality reduction, features selection, and tool wear prediction in challenging CNC machining domains and materials, with a case study conducted on Inconel 718. This provides evidence of a possible on-going exploration of other high-performance aerospace materials, such as Waspaloy, Titanium, and fiber-reinforced composites. Moreover, continued investigation of the model's generalization could enhance its significant application across various manufacturing industries. In the meantime, rigorous online experiments are needed to validate the versatility and reliability of the multi-sectional SVD-based ML technique in predicting VB and RUL across various CNC machining operations, tools, and workpiece materials. Furthermore, the integration of this system with emerging technologies such as the Internet of Things (IoT) can enable adaptive monitoring and control of tool wear evolution in challenging CNC machining domains. This integration ushers in a new era of transformative machining practices during intelligent manufacturing of superalloy components.

Author contribution All authors contributed to the conceptual idea of the manuscript. The first draft of the manuscript was written by Dr. Tiyamike Banda. All authors commented on the previous versions. Dr. Veronica Lestari Jauw, Assoc. Prof. Ali Akhavan Farid, Prof. Chuan Li, and Assoc. Prof. Chin Seong Lim supervised, reviewed, and edited the manuscript. All authors read and finally approved the final version of the manuscript.

Data availability The data used in this manuscript is available from the corresponding author and can be accessed on reasonable request.

Code availability Not applicable.

Declarations

Ethics approval Not applicable because this article does not contain any studies with human or animal subjects.

Consent to participate Not applicable.

Consent for publication Not applicable.

Competing interests The authors declare no competing interests.

References

1. Polvorosa R, A Suárez L. de Lacalle, I. C.-J. of M, undefined 2017, Tool wear on nickel alloys with different coolant pressures: comparison of Alloy 718 and Waspaloy, Elsevier, Accessed: Sep. 01, 2020. [Online]. Available: https://www.sciencedirect.com/science/article/pii/S1526612517300129

2. Anderson M, Patwa R, Shin YC (2006) Laser-assisted machining of Inconel 718 with an economic analysis. Int J Mach Tools Manuf 46(14):1879–1891. https://doi.org/10.1016/j.ijmachtools.2005.11.005

3. Banda T, Jie BYW, Farid AA, Lim CS (2022) Machine vision and convolutional neural networks for tool wear identification and classification 737–747. https://doi.org/10.1007/978-981-33-4597-3_66.

4. Wu X, Liu Y, Zhou X, Mou A (2019) Automatic identification of tool wear based on convolutional neural network in face milling process. Sensors (Switzerland) 19(18). https://doi.org/10.3390/s19183817.

5. ISO 8688-1: (1989) (E) Tool life testing in milling - Part 1: face milling. International organization for standardization

6. Banda T, Liu Y, Farid AA, Lim CS (2023) A machine learning model for flank wear prediction in face milling of Inconel 718. Int J Adv Manuf Technol. https://doi.org/10.1007/s00170-023-11152-3

7. Banda T, Jauw VL, Farid AA, Wen NH, Xuan KCW, Lim CS (2023) In-process detection of failure modes using YOLOv3-based on-machine vision system in face milling Inconel 718. Int J Adv Manuf Technol 3885–3899. https://doi.org/10.1007/s00170-023-12168-5.

8. Ong P, Lee WK, Lau RJH (2019) Tool condition monitoring in CNC end milling using wavelet neural network based on machine vision. Int J Adv Manuf Technol 104(1–4):1369–1379. https://doi.org/10.1007/s00170-019-04020-6

9. Zhu K (2022) Machine vision based smart machining system monitoring. 267–295. https://doi.org/10.1007/978-3-030-87878-8_8

10. Pontevedra V et al (2018) ScienceDirect ScienceDirect ScienceDirect Tool wear prediction in end milling of Ti-6Al-4V through Kalman Tool wear prediction in end milling of Ti-6Al-4V through Kalman filter based fusion of International texture features and cutting forces filter based. Procedia Manuf 26:1459–1470. https://doi.org/10.1016/j.promfg.2018.07.095

11. Castejón M, Alegre E, Barreiro J, Hernández LK (2007) On-line tool wear monitoring using geometric descriptors from digital images. Int J Mach Tools Manuf 47(12–13):1847–1853. https://doi.org/10.1016/j.ijmachtools.2007.04.001

12. Prasad KN, Ramamoorthy B (2001) Tool wear evaluation by stereo vision and prediction by artificial neural network. J Mater Process Technol 112(1):43–52. https://doi.org/10.1016/S0924-0136(00)00896-7

13. Wu X, Liu Y, Zhou X, Mou A (2019) Automatic identification of tool wear based on convolutional neural network in face milling process. Sensors (Switzerland) 19(18). https://doi.org/10.3390/s19183817

14. Banda T, Lestari V, Chuan J, Ali L, Farid A, Seong C (2022) Flank wear prediction using spatial binary properties and artificial neural network in face milling of Inconel 718. Int J Adv Manuf Technol 0123456789. https://doi.org/10.1007/s00170-022-09039-w

15. Banda T, Ho KY, Akhavan Farid A, Lim CS (2021) Characterization of tool wear mechanisms and failure modes of TiAlN-NbN coated carbide inserts in face milling of Inconel 718. J Mater Eng Perform no. Ref 10. https://doi.org/10.1007/s11665-021-06301-2

16. Li L, An Q (2016) An in-depth study of tool wear monitoring technique based on image segmentation and texture analysis. Meas J Int Meas Confed 79:44–52. https://doi.org/10.1016/j.measurement.2015.10.029

17. Devillez A, Lesko S, Mozer W (2004) Cutting tool crater wear measurement with white light interferometry. Wear 256(1–2):56–65. https://doi.org/10.1016/S0043-1648(03)00384-3

18. Karthik A, Chandra S, Ramamoorthy B, Das S (1997) 3D tool wear measurement and visualisation using stereo imaging. Int J Mach Tools Manuf 37(11):1573–1581. https://doi.org/10.1016/S0890-6955(97)00023-0

19. Banda T, Farid AA, Li C, Jauw VL, Lim CS (2022) Application of machine vision for tool condition monitoring and tool performance optimization–a review. Int J Adv Manuf Technol 121(11):7057–7086. https://doi.org/10.1007/s00170-022-09696-x

20. Kolev V, Tsvetkova K, Tsvetkov M (2010) Singular value decomposition of images from scanned photographic plates. VII Serbian-Bulgarian Astron Conf SBAC 2010(11):187–200

21. Sadek RA (2020) SVD based image processing applications: state of the art, contributions and research challenges, 2012. [Online]. Available: www.ijacsa.thesai.org. Accessed: Sep. 06, 2020

22. Andrews HC, Patterson CL (1976) Singular value decompositions and digital image processing. IEEE Trans Acoust 24(1):26–53. https://doi.org/10.1109/TASSP.1976.1162766

23. Konstantinides K, Natarajan B, Yovanof GS (1997) Noise estimation and filtering using block-based singular value decomposition. IEEE Trans Image Process 6(3):479–483. https://doi.org/10.1109/83.557359

24. Anowar F, Sadaoui S, Selim B (2021) Conceptual and empirical comparison of dimensionality reduction algorithms (PCA, KPCA, LDA, MDS, SVD, LLE, ISOMAP, LE, ICA, t-SNE). Comput Sci Rev 40. https://doi.org/10.1016/j.cosrev.2021.100378

25. Cirillo MD, Mirdell R, Sjöberg F, Pham TD (2019) Tensor decomposition for colour image segmentation of burn wounds. Sci Rep 9(1):1–13. https://doi.org/10.1038/s41598-019-39782-2

26. Kaya B, Oysu C, Ertunc HM (2011) Advances in Engineering Software Force-torque based on-line tool wear estimation system for CNC milling of Inconel 718 using neural networks. Adv Eng Softw 42(3):76–84. https://doi.org/10.1016/j.advengsoft.2010.12.002

27. Faghih Dinevari V, Karimian Khosroshahi G, Zolfy Lighvan M (2016) Singular value decomposition based features for automatic tumor detection in wireless capsule endoscopy images. Appl Bionics Biomech 2016. https://doi.org/10.1155/2016/3678913

28. Liu J, Niu X, Kong W (2006) Image watermarking based on singular value decomposition. Proc. - 2006 Int. Conf. Intell. Inf. Hiding Multimed. Signal Process. IIH-MSP. 457–460. https://doi.org/10.1109/IIH-MSP.2006.265040

29. Arif J, Chaudhuri NR, Ray S, Chaudhuri B (2009) Online Levenberg-Marquardt algorithm for neural network based estimation and control of power systems. Proc Int Jt Conf Neural Networks 199–206. https://doi.org/10.1109/IJCNN.2009.5179071

30. Thakre AA, Lad AV, Mala K (2019) Measurements of Tool wear parameters using machine vision system. https://doi.org/10.1155/2019/1876489

31. Mikołajczyk T, Nowicki K, Kłodowski A, Pimenov DY (2016) Neural network approach for automatic image analysis of cutting edge wear. Mech Syst Signal Process 88:100–110. https://doi.org/10.1016/j.ymssp.2016.11.026

32. Ezugwu EO, Wang ZM, Machado AR (2000) Wear of coated carbide tools when machining nickel (Inconel 718) and titanium base (Ti-6A1-4V) alloys. Tribol Trans 43(2):263–268. https://doi.org/10.1080/10402000008982338

33. De Melo ACA, Milan JCG, Da Silva MB, Machado ÁR (2006) Some observations on wear and damages in cemented carbide tools. J Brazilian Soc Mech Sci Eng 28(3):269–277. https://doi.org/10.1590/s1678-58782006000300004